buildings

MDPI

Article

Geometric Imperfection Simulations in Cee-Shape Cold-Formed Steel Members Based on Newly Developed Machine-Vision Inspection Techniques

Hanbo Guan [1], Xi Zhao [2,*], Pengfei Du [2] and Xiaoyan Sun [2]

[1] Beijing Intelligent Prefabricated Building Research Institute, Beijing 100071, China
[2] School of Civil and Transportation Engineering, Beijing University of Civil Engineering and Architecture, Beijing 100044, China
* Correspondence: zhaoxi@bucea.edu.cn; Tel.: +86-189-0235-8188

Abstract: This paper insightfully studies geometric imperfection simulations of cee-section CFS members from laser-based measurements. A machine-vision imperfection inspection technique is first developed where an algorithm is implemented to automate imperfection characterization from volumetric data. The measured imperfections are statistically analyzed and resemble past measurements from other researchers. Two imperfection simulation approaches are studied, i.e., the modal imperfection simulation method and the 1D spectral simulation method, where strength performance and deformation are predicted from finite element analysis. The analysis results are compared with those of testing. The 1D spectral simulation method is superior where stochasticity and regularity of real im-perfection can be properly addressed. The study provides feasible access to imperfection simulations of cee-section CFS members that other researchers can directly apply. The prediction results can aid the future direct analysis and design of CFS members.

Keywords: geometric imperfection; machine vision measurement; smart imperfection characterization; digital twin; imperfection simulation

Citation: Guan, H.; Zhao, X.; Du, P.; Sun, X. Geometric Imperfection Simulations in Cee-Shape Cold-Formed Steel Members Based on Newly Developed Machine-Vision Inspection Techniques. *Buildings* **2023**, *13*, 2786. https://doi.org/10.3390/buildings13112786

Academic Editor: Hiroshi Tagawa

Received: 31 August 2023
Revised: 26 October 2023
Accepted: 1 November 2023
Published: 6 November 2023

1. Introduction

Cold-formed steel (CFS) is used extensively in low- to mid-story structures due to its lightweight nature and ease of erection. However, due to its thin-walled character it is very sensitive to geometric imperfections [1]. These geometric imperfections are generated randomly at various stages, including manufacturing, transportation, storage, and the erection of CFS members [2]. Historically, the performance of CFS members has been estimated using the empirical equations proposed by Winter [3]. However, with the advancements in computational and analytical techniques over the past decade, the design of CFS structures has evolved, and now they require more than just implicit consideration of geometric imperfections through empirical corrections in strength design equations [4,5]. There is a need for simulations to represent the characteristics and stochasticity of geometric imperfections more accurately in CFS members [6–9]. A satisfactory simulation must be grounded in comprehensive research to identify imperfections, and the research must range from the acquisition of data to the characterization of imperfect patterns and from the analysis of data to the selection of simulation approaches.

The acquisition of data is the initial challenge in studying the geometric imperfections in CFS structural members. Measurement techniques have undergone significant advancements over the past few decades, transitioning from contact to non-contact methods [8,10]. Contact measurement techniques, such as the Linear Variable Displacement Transducer (LVDT), displacement sensors, and calipers, traditionally have been used to survey surface deviations in geometric imperfections [11–13] However, these conventional methods have limitations that hinder the full-field geometric measurement of CFS members. For

instance, it is problematic to assess the corners of cross-sections with these methods [1]. Also, the time-intensive nature of current methods has led to relatively small databases. Also, there is a need for high-throughput methods to extend the imperfection measurements made in laboratories to manufacturing facilities for the purpose of quality control. These limitations have prompted interest in full-field, non-contact measurement techniques for thin-walled structural members. McAnallen et al. (2014) [14] and Zhao and Schafer (2015) [1] introduced non-contact methods, such as photogrammetry and laser triangulation techniques. However, photogrammetry cannot provide thorough, high-throughput, geometric information for imperfection studies at an economic cost [9]. The non-contact geometric imperfection measurements are prone to be laser measurement techniques. Laser measurement techniques have developed from the inconvenient platform to the flexible hand-held scanner [1,6,15,16]. The requirements for effectiveness and thoroughness of data acquisition in geometric imperfections are therefore satisfied.

Imperfection simulations encounter a second challenge in the characterization or identification of geometric imperfections, which are inherently random along a member. The characterization aims to find patterns of the imperfections that affect the strength and deformation of cold-formed steel members. A conventional database of imperfections, as it existed then, was assembled by Schafer and Pekoz [11], and classified geometric imperfections into two primary categories, i.e., Type 1 (d1) and Type 2 (d2) based on the plate's 'out-of-flatness' and 'out-of-straightness'. J.R. Vieira et al. [15] (2011) expanded upon this work by measuring global and cross-section imperfections across a range of channel sections. They used a position transducer on a manual linear stage to gauge global imperfections across various sections of a channel. Further, Zeinoddini and Schafer (2011) [6] refined the characterization of the available imperfections into global imperfections and cross-section imperfections, which encompassed bow (G1), camber (G2), and twist (G3), as well as the Type 1 (d1) and Type 2 (d2) imperfections that were mentioned previously. However, the categorizations of Type 1 (d1) and Type 2 (d2) imperfections proved to be insufficient in capturing the nuances of cross-sectional imperfections [17]. Modal imperfection characterization is proposed based on the modal identification method proposed by Li [18]. A more nuanced approach, focusing on the shapes of local and distortional buckling modes, was found to pinpoint the imperfection vulnerabilities of CFS members [19]. Although some researchers [9,16,20] have proposed an imperfection characterization method to deal with structural members, the automatic imperfection characterization and inspections that are based on modal imperfections have not been formulated and detailed. Zhao only states the characterization of Type 1, Type 2, and global imperfections, and Xu's method cannot accommodate the rounded corners of CFS members. Burcu proposed methods in which discrete points on the cross sections of the CFS members are analyzed. An automated and thorough characterization of the geometric imperfection of CFS members should be adapted to the volumetric data from the laser scanners.

Imperfection simulations are important elements in the study of geometric imperfections on CFS members. Several researchers have proposed various methods for establishing the simulations. The most extensively used method is first-mode imperfection simulations, which only considers global imperfections [8,10]. However, the results of the characterization shows that first-mode imperfection simulations cannot account for the performance of short and medium-length compression members. Thus, modal imperfection simulations [21] and 1D spectral methods [6] are proposed. However, the shortage of cross-section geometric information and lack of experimental validation restricts the application of these simulation approaches. The direct simulation method steps onto the stage with the development of laser scanning techniques. Researchers proposed different data-driven methods with machine learning from an abundance of full-field geometric data of CFS members [9]. Though these methods can better predict performance of CFS members, a large number of measurements are required for the machine learning process which are difficult to obtain in practice.

This paper improves the laser-based imperfection measurement method with a machine-vision inspection technique where automatic imperfection inspection is performed without manual operations. The imperfection inspection characterizes those mode imperfections to which the strength of CFS members is sensitive. The characterized mode imperfections are then statistically analyzed, with results that resemble historic measurements. Results show that the probability models of mode imperfections are capable of general simulations of cee-section CFS members. Two imperfection simulation methods, i.e., 1D spectral and modal imperfection, are applied towards the characterized imperfections from machine-vision inspection techniques. Both methods are compared with experimental results, showing that 1D spectral simulation is more proper and feasible with the newly developed techniques. Furthermore, the mode imperfection contributions to strength of CFS members are analyzed for better understanding the significance of geometric imperfections.

The background of this research is introduced in Section 2. The automation algorithm of imperfection characterization for machine-vision inspection techniques is detailed in Section 3. Section 4 demonstrates the modified 1D spectral methods with a comparison with traditional modal imperfection simulations, which are validated through the experimental results. The contribution of different imperfection modes is discussed in Section 5 and concluding remarks are made in Section 6.

2. Background of Imperfection Study

2.1. The Laser Measurements Setup

The research conducts a geometric imperfection analysis using a laser-based machine-vision technique. This method involves a hand-held laser scanner capturing detailed measurements of CFS members. The collected measurement point clouds undergo post-processing via an optimization-based robust feature recognition algorithm [9]. This process yields digital twins of the CFS members' geometries, enabling comprehensive and automated identification of imperfections directly from the measurements.

Measurements are obtained using the EinScan HX (Beijing Tian yuan 3D Technol-ogy Co., Ltd., Beijing, China), a handheld 3D scanner equipped with a hybrid blue laser and LED light source. This class 1 eye-safe laser scanner boasts a precision of up to 0.04 mm. With a working distance of 470 mm, it can capture an area as large as 380 mm × 400 mm. Despite its ability to scan specimens up to 5 m long, its volumetric accuracy remains within 0.5 mm. Given its handheld design, the scanner offers flexibility. A specimen is first placed on a steel frame for scanning. The steel frame holding the specimen may cover a small part of the scanned specimen where the missing data are later patched up from the software. The specimens are stuck with unique markers for the scanning registration from multiple scans, as illustrated in Figure 1a. The aligned scan data are subsequently processed using software (Geomagic version 2013.0.2 [Computer software]. Geomagic, Inc., Research Triangle Park, NC, USA and 3Dsystems. Inc. Mole, Rock Hill, SC, USA) supplied by EinScan HX [22]. After removing noise from the point clouds, the CFS member's clean point cloud model is obtained, as depicted in Figure 1b.

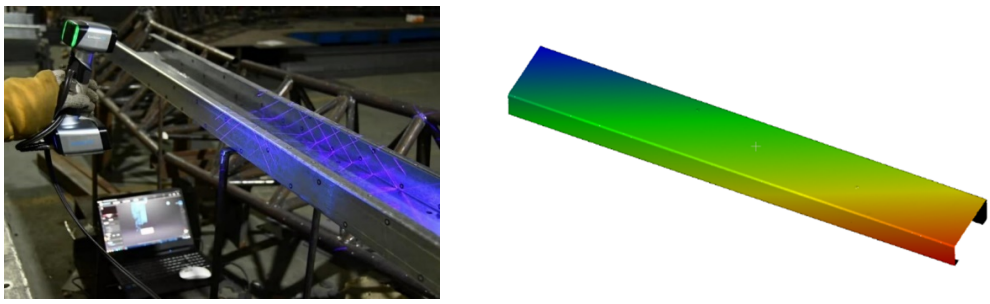

(**a**) (**b**)

Figure 1. Laser measurements: (**a**) Scanning process; (**b**) A typical point-cloud model.

The point cloud models of CFS members subsequently undergo segmentation and post-processing using an optimization-based robust feature recognition algorithm [9]. This algorithm adeptly and swiftly identifies features of diverse section types of CFS members, as illustrated in Figure 2. Concurrently, the point-cloud models are reorganized and restructured. This reconfiguration facilitates the easy extraction of geometric data, such as dimensions and imperfections, for in-depth analysis.

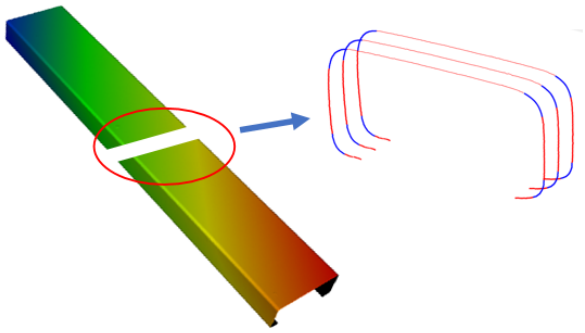

Figure 2. Reconstruction of CFS members.

2.2. Scheme of Specimens

The study investigates a bunch of cee-section CFS members through a machine-vision imperfection inspection technique. The imperfections of cee-section members are studied where data are applied in simulations of imperfection. The cee-section members in the data scheme are typically used in thin-walled structures in China (see Table 1). Each section type of CFS member has three specimens. Overall, the study covers 27 section types and encompasses 81 CFS members. The dimensions of these members are listed below, with illustrations in Figure 3a.

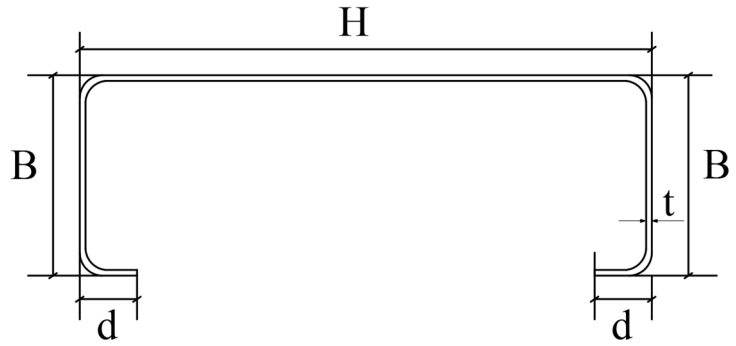

(**a**)

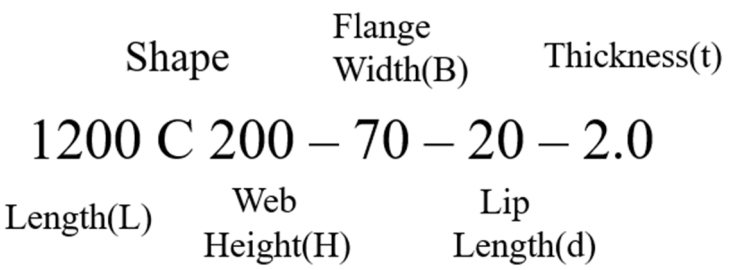

(**b**)

Figure 3. Illustration of CFS member. (**a**) Dimensional diagram of CFS; (**b**) Notation of the section name.

Table 1. Data scheme of Geometric imperfection study.

Type	Section Type	H(mm) [(a)]	B(mm) [(a)]	d(mm) [(a)]	t(mm) [(a)]
1	450C180-70-20-2.0 [(b)]	180.00	70.00	20.00	2.00
2	450C180-70-20-2.5	180.00	70.00	20.00	2.50
3	450C180-70-20-3.0	180.00	70.00	20.00	3.00
4	450C200-70-20-2.0	200.00	70.00	20.00	2.00
5	450C200-70-20-2.5	200.00	70.00	20.00	2.50
6	450C200-70-20-3.0	200.00	70.00	20.00	3.00
7	450C280-70-20-2.0	280.00	70.00	20.00	2.00
8	450C280-70-20-2.5	280.00	70.00	20.00	2.50
9	450C280-70-20-3.0	280.00	70.00	20.00	3.00
10	1200C180-70-20-2.0	180.00	70.00	20.00	2.00
11	1200C180-70-20-2.5	180.00	70.00	20.00	2.50
12	1200C180-70-20-3.0	180.00	70.00	20.00	3.00
13	1200C200-70-20-2.0	200.00	70.00	20.00	2.00
14	1200C200-70-20-2.5	200.00	70.00	20.00	2.50
15	1200C200-70-20-3.0	200.00	70.00	20.00	3.00
16	1200C280-70-20-2.0	280.00	70.00	20.00	2.00
17	1200C280-70-20-2.5	280.00	70.00	20.00	2.50
18	1200C280-70-20-3.0	280.00	70.00	20.00	3.00
19	3000C180-70-20-2.0	180.00	70.00	20.00	2.00
20	3000C180-70-20-2.5	180.00	70.00	20.00	2.50
21	3000C180-70-20-3.0	180.00	70.00	20.00	3.00
22	3000C200-70-20-2.0	200.00	70.00	20.00	2.00
23	3000C200-70-20-2.5	200.00	70.00	20.00	2.50
24	3000C200-70-20-3.0	200.00	70.00	20.00	3.00
25	3000C280-70-20-2.0	280.00	70.00	20.00	2.00
26	3000C280-70-20-2.5	280.00	70.00	20.00	2.50
27	3000C280-70-20-3.0	280.00	70.00	20.00	3.00

Note: (a) H is web height, B is flange width, d is lip length, and t is thickness. (b) Each type of member has three specimens.

The notation for the section name is shown in Figure 3. Here, the first number represents the length of the CFS members. The letter 'C' denotes the shape of a member. Subsequent numbers represent the web height, flange width, lip height, and thickness, respectively. All these measurements are provided in millimeters.

2.3. Experimental Setup for Validation

The imperfection simulation is validated through the experimental results. Axial compression testing is conducted on the specimens described in Table 1, whereby loading capacities and deformations are obtained for validation. The cee-section CFS members are installed in the reaction frame using articulated clamps (Figure 4). The articulated supports imitate simple supports for better understanding the impacts of imperfections. A 50-ton actuator is mounted and provides axial compression of tested members.

The testing is controlled by loads at the early testing stage and by displacements when maximum capacity is achieved. The details of testing procedures and material testing can be found from the previous research [23].

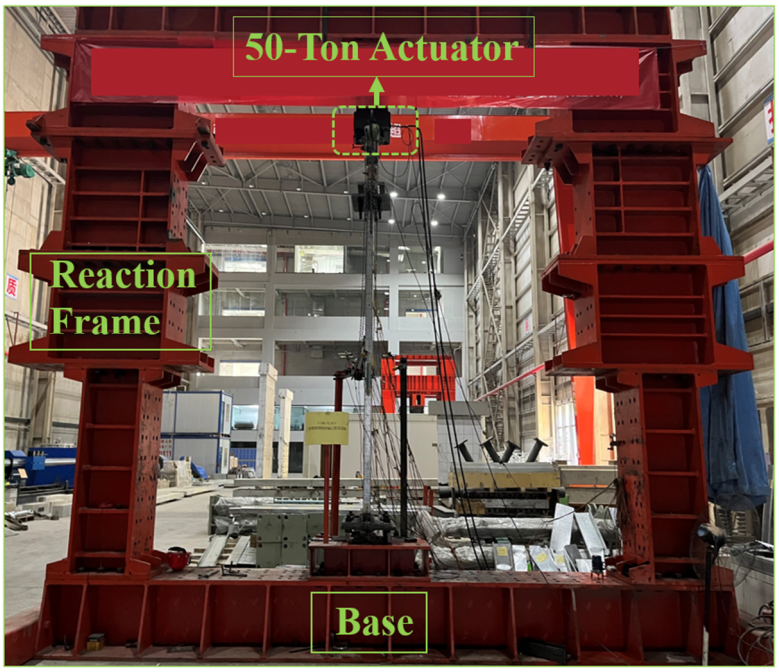

Figure 4. Experimental setup.

3. Analysis of Imperfections

3.1. Automatic Imperfection Characterization

The machine-vision imperfection inspections are composed of hardware and software components. The hardware typically involves high-throughput optical measurement devices, such as laser scanners, which are already well-developed. The software, however, still requires further research for efficient processing of the large volume of point clouds of CFS members, as shown in Figure 1b. To address this, an automatic imperfection characterization algorithm has been developed. This algorithm complements the machine-vision imperfection inspections system by automating the extraction of imperfections from the point clouds of CFS members.

The first step in the algorithm is to determine the shapes of mode imperfections. Mode imperfections, like buckling modes, are considered to have a very significant impact on the strength of CFS members [2]. These mode imperfections are classified into cross-sectional and global categories. Cross-sectional imperfections include local and distortional types, as depicted in Figure 5a,b. Global imperfections, conversely, consist of bow (G1), camber (G2), and twist (G3) imperfections, as shown in Figure 5c–e.

The second step of the algorithm is to find the magnitudes and shape functions corresponding to specific imperfection modes, as represented in Equation (1):

$$P(z) = \sum \alpha_i(z)\Phi_i(z) \quad (1)$$

where:

$P(z)$: represents surface deviations;
i: represents imperfection modes such as local, distortional, G1, G2, G3;
α: magnitudes of imperfections;
Φ: shape function associated with mode imperfections;
z: the longitudinal position along a CFS member.

In alignment with the characteristics of mode imperfections, the smart automatic imperfection characterization is divided into two parts: one for global mode imperfections and another for cross-sectional mode imperfections. The first part focuses on identifying global mode imperfections. Generally, these global imperfections are rigid and independent of each other. The magnitudes of G1 and G2 imperfections can be easily determined by

evaluating the deviations from the centroids of cross-sections along the longitudinal axis, as depicted in Figure 6. The magnitudes of G3 imperfections are estimated based on the web rotation relative to the nominal cross-sections.

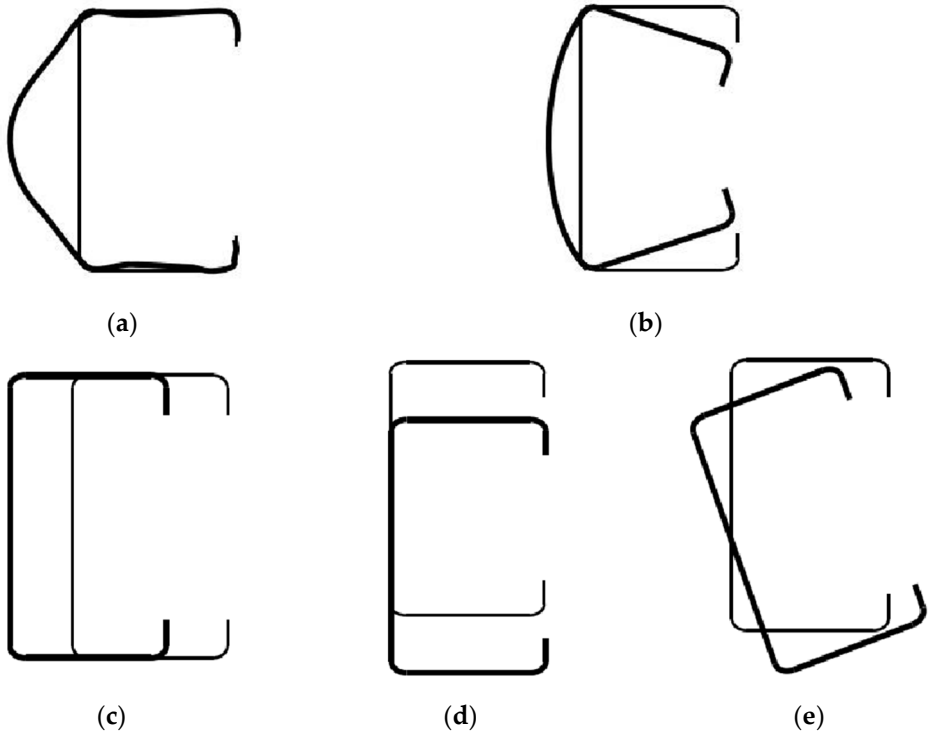

Figure 5. Imperfection modes [6]: (**a**) Local; (**b**) Distortional; (**c**) Bow; (G1); (**d**) Camber; (G2); (**e**) Twist (G3).

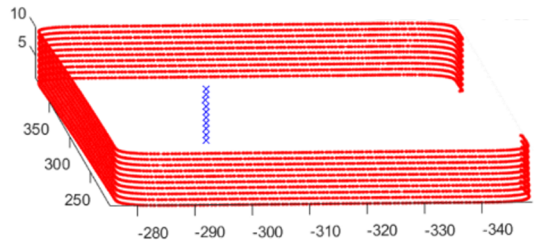

Figure 6. Centroids calculation from the DT of CFS members.

Local and distortional mode imperfections present a somewhat complex scenario. Firstly, cross-sectional imperfections (δ) are derived by comparing the measured profiles to the nominal cross-sections. However, these imperfections inherently consist of both local and distortional modes coupled together. Thus, a decoupling process becomes indispensable. The shapes of these two modes can be determined using CUFSM. At the signature curve of the CFS member, two local minimum strength coefficients pertaining to local and distortional buckling can be identified (Figure 7). The associated deformation shapes of the cross-sections are designated as φs. Subsequently, the magnitudes of the local and distortional imperfections can be determined using Equations (2) and (3).

$$S_{err} = (\alpha\varphi - \delta)^T(\alpha\varphi - \delta) \tag{2}$$

$$\alpha = \left(\varphi^T\varphi\right)^{-1}\left(\varphi^T\delta\right) \tag{3}$$

where S_{err} represents the square error.

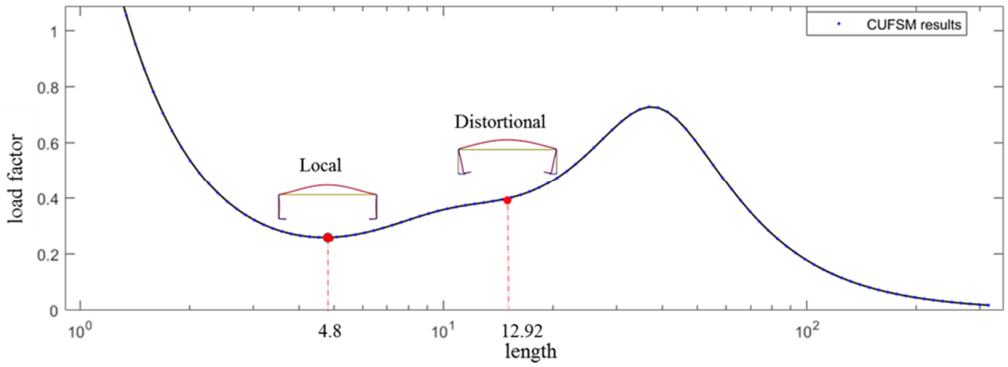

Figure 7. Local and distortional mode shapes derived from the signature curve in CUFSM (The blue represents undeformed shape, the red represents deformed shape).

3.2. Results of Mode Imperfection Characterization

The mode imperfections are characterized from a total of 81 cee-section specimens, described in Table 1. Imperfections are observed independently of cross-section sizes which are normalized for further computation. Considering that the strength of CFS members is sensitive to the length of the member, statistical analysis is conducted with respect to length of specimens, i.e., 450 mm, 1200 mm, and 3000 mm, as shown in Table 2. The number of specimens is 27 per section group. The mode imperfection is characterized cross-section by cross-section of a member. Thus, the sample size of mode imperfections varies with the length of members. The longitudinal resolution of imperfection is 3 mm. The overall sample sizes of mode imperfection are 4050, 10,800, and 27,000 with respect to lengths 450 mm, 1200 mm, and 3000 mm from Equation (4).

$$\text{sample size} = \text{member sample size} \times \frac{\text{cross section}}{\text{member}} \tag{4}$$

The statistical results, mean and standard deviations, are presented in Table 2. The measurements are compared with the past measurements P_{hist1} and P_{hist2} from past researchers. As some researchers only have global or cross-section mode imperfections, the comparisons between cross-section and global mode imperfections are presented in Table 2a,b, respectively. The local and distortional mode imperfections appear to be unrelated to the length of members. In fact, these cross-sectional imperfections are more strongly influenced by the web height. An increase in web height exacerbates local imperfections while reducing distortional imperfections. As for global imperfections, their magnitudes seem independent of length and web height. The average values for G1 and G2 are L/4411 and L/5405, respectively. The average twist, G3, is 0.12°/L, which also appears to be independent of web height and member length.

When comparisons are made between the machine-vision inspection and the past measurements, it is observed that the differences in local and distortional mode imperfections are small. This implies that the measurements are feasible for general application in simulations. On the other hand, the global mode imperfections show around 30% similarity in G2 and G3 modes. The G1 mode, however, is slightly smaller than the that of past measurements. However, both G1 mode imperfections are smaller than standards requirements [24,25].

Table 2. (**a**) Statistical analysis of cross-section mode imperfections. (**b**) Statistical analysis of global mode imperfections.

(a)		
	Mode Imperfections	
Section Group	**Local** (δ_l/t)	**Distortional** (δ_d/t)
P_{L450}	0.15	0.22
P_{L1200}	0.21	0.48
P_{L3000}	0.18	0.43
Mean (μ_{P_L})	0.19	0.42
Standard deviations (σ_{P_L})	0.01	0.17
P_{hist1} (a)	0.24	0.39
% difference (c)	27.69%	6.89%

(b)			
Section Group	**G1** (L/δ_{G1})	**G2** (L/δ_{G2})	**G3** $\left(^{\circ}/L\right)$
P_{L450}	3200	3138	0.16
P_{L1200}	4489	5542	0.11
P_{L3000}	4561	5690	0.12
Mean (μ_{P_L})	4411	5405	0.12
Standard deviations (σ_{P_L})	3177	3951	0.05
P_{hist2} (b)	2133	3361	0.15
% difference(c)	51.65%	37.80%	27.78%

Note: (a) P_{hist1} is the mean of cross-section measurements from researchers [26–28]. The sample sizes are 89, 12, and 30, respectively. (b) P_{hist2} is the mean of global measurements from researchers [6,26,28]. The sample sizes are 89, 210, and 30, respectively. (c) % difference $= \left| \frac{\mu_{P_L} - P_{hist}}{\mu_{P_L}} \right|$.

3.3. Results of Mode Imperfection Characterization

Spectral analysis is performed on the imperfections of CFS members using the Fast Fourier Transform (Equation (5)), as described in Zhao's article [19]. The imperfection spectrum is generated for all members.

It is observed that spectrum curves with different lengths show similarity. Typical 1D spectral curves for mode imperfections are illustrated in Figure 8. The curves' horizontal axis represents the half-wavelength's reciprocal, while the vertical axis represents the energy corresponding to each half-wavelength of a given mode imperfection. The results indicate that the spectrum primarily governs global imperfections at the lowest frequency (1/L), which aligns with general assumptions in imperfection modeling. Conversely, local imperfections appear to be composed of multiple spectra at various frequencies. Distortional imperfections behave similarly to global imperfections.

The typical spectral curves can be statistically analyzed and form base spectral curves, which are used to simulate imperfections as discussed in Section 4.2.

$$Y = FFT(X, N) \tag{5}$$

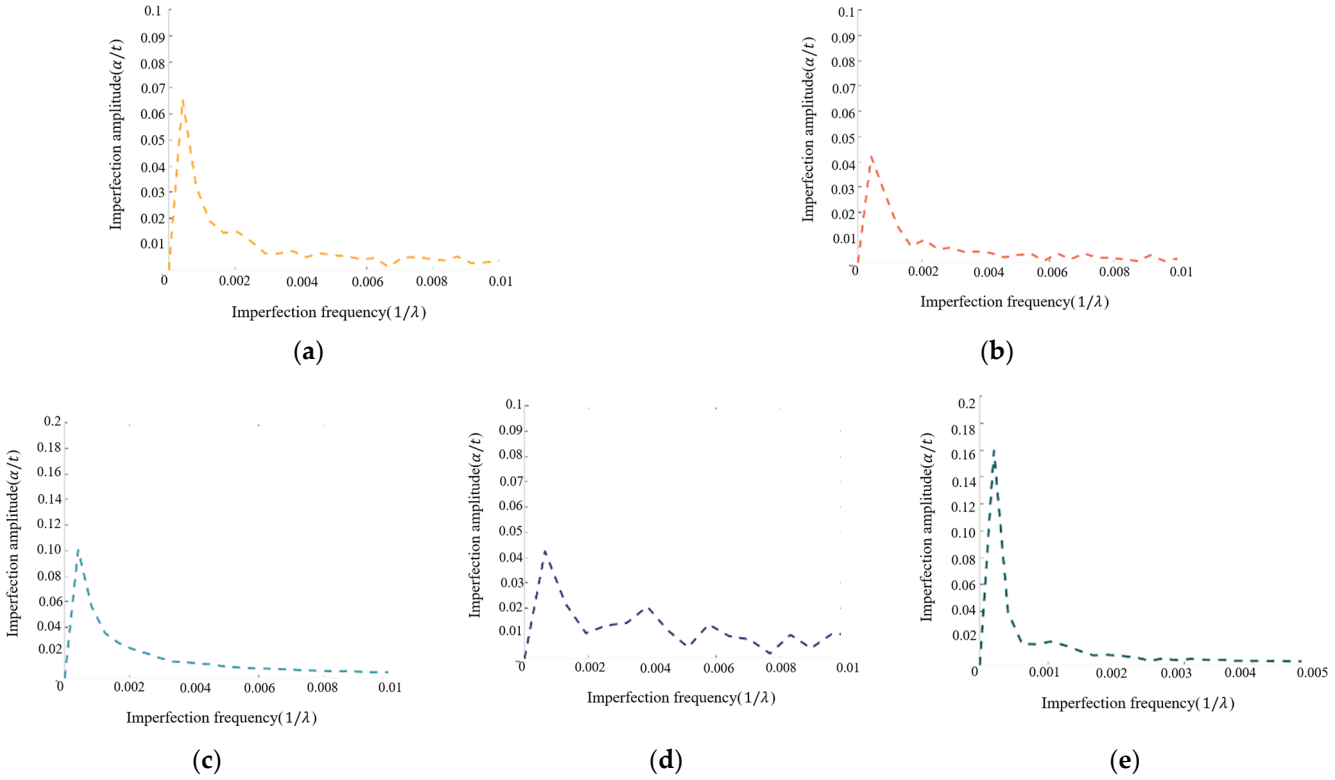

Figure 8. Typical spectral curves of geometric imperfections of a member: (**a**) G1; (**b**) G2; (**c**) G3; (**d**) D1; (**e**) D2.

4. Simulation of Imperfections

The simulations of imperfections target the prediction of structural performance of a CFS member with easiness and efficiency. The simulation methods are discussed in this section, i.e., the traditional modal imperfection method and the 1D spectral method. Detailed procedures for simulations using characterized mode imperfections from the newly developed technique are discussed. The simulations are then validated through experimental results [21].

4.1. Traditional Simulation Approaches

The traditional method for simulating imperfections generally assumes that linear superposition of mode imperfections can be performed, typically using Equation (6). In this approach, different mode imperfections are combined using a coefficient of imperfection characteristics, denoted as c_i. These mode imperfections are composed of a constant magnitude α_i (as per Equation (7)) and a shape function ϕ_i. Given the stochastic nature of actual imperfections, simulations for both magnitudes and coefficients are conducted using probabilistic methods where the probabilistic models are obtained from Section 3.2.

$$P(z) = \sum_{i=1}^{n} c_i \alpha_i \phi_i(x, y, z) \tag{6}$$

$$\phi_i(x, y, z) = \xi_i \sin\left(\frac{1}{\lambda_i} z\right) \tag{7}$$

where:

i: denotes the mode of imperfection, which could be local, distortional, G1, G2, or G3;
c_i: represents the coefficient of imperfection characteristics, with possible values of -1, 0, or 1;

α_i: refers to the magnitudes of the corresponding imperfection mode i along the length of a CFS member;
ξ_i: denotes the normalized cross-section mode shape for imperfection mode i;
ϕ_i: represents the shape function corresponding to imperfection mode i;
λ_i: indicates the half-wavelength of a sinusoidal wave corresponding to a mode imperfection;
z: Specifies the longitudinal coordinates of a CFS member.

(a) Magnitudes α_i

The genuine imperfections in materials can be attributed to factors such as manufacturing, storage, and transportation processes. The magnitudes of these imperfections predominantly signify the inherent stochasticity of real-world geometric imperfections. Such stochasticity is gleaned from the statistical analysis of imperfection measurements, as depicted in Figure 9. This analysis reveals that these imperfections closely align with the Gaussian distribution, represented as $P \sim G(\mu, \sigma)$. The mean μ and standard deviation σ extracted from the mode imperfection magnitudes are subsequently utilized to construct a probabilistic model of magnitudes α. This model, denoted as $F(\hat{\mu}, \hat{\sigma})$, is premised upon a normal distribution. Random sampling is then executed based on the probabilistic model $F(\hat{\mu}, \hat{\sigma})$. It is essential to note that $\hat{\mu} = \mu$, and $\hat{\sigma} = \sigma$. The values can be found from Table 2 for the simulations.

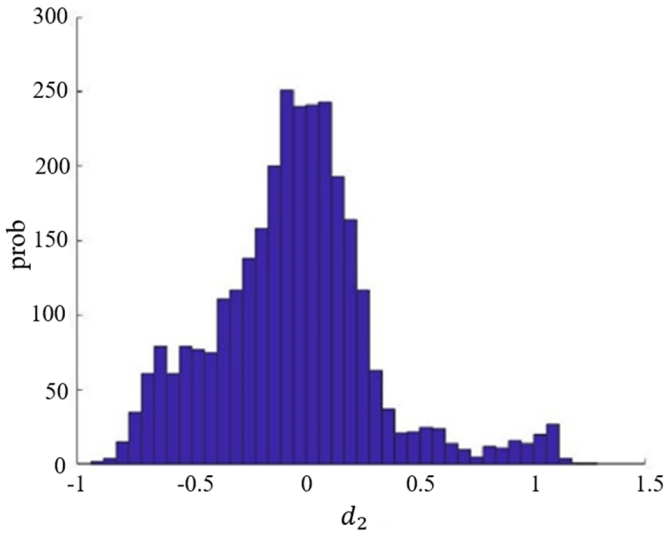

Figure 9. Histogram of mode imperfections based on DT measurements.

(b) Shape function ϕ_i

The shape function, ϕ_i, characterizes the longitudinal distribution of a mode imperfection. In the conventional approach (as expressed in Equation (6)), ϕ_i is typically approximated as a scaled sinusoidal function. This function's frequency is determined by the inverse of the half-wavelength, λ, corresponding to buckling. The scaling factors originate from the associated cross-sectional buckling modes, φ_i. Consequently, for global mode imperfections, λ_G matches the total length of a member, denoted as L, as illustrated in Figure 10. In contrast, the local and distortional mode imperfections possess half-wavelengths, λ_L and λ_D, which equate to those of the local and distortional buckling as determined by CUFSM. This suggests that mode imperfections maintain consistent shape functions in the conventional imperfection simulation, and the imperfection shapes resemble buckling.

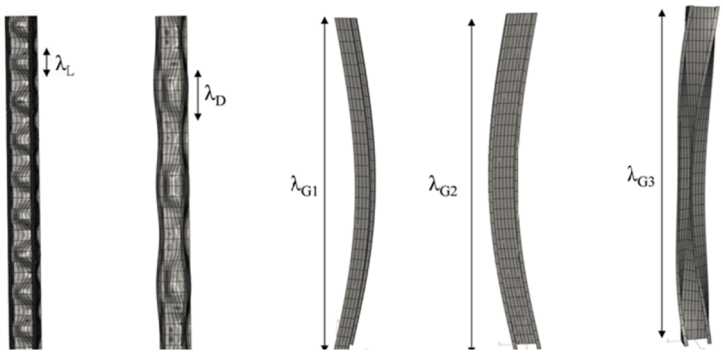

Figure 10. Imperfection simulations using the traditional approach [6].

(c) Coefficient of imperfection characteristics c_i

The coefficient of imperfection characteristics, c_i, serves as the weight for each mode imperfection during the process of linear superposition. Given that the magnitudes α_i are stochastically simulated to represent the values of imperfections, c_i is better suited for indicating the directions of these mode imperfections. Specifically, c_i can take one of the following values: -1, 0, or 1.

Mode imperfections are assumed to be statistically independent when incorporating the imperfections characteristics, c_i. As a result, c_i follows a uniform distribution and is subject to random sampling.

Upon completion of the traditional imperfection simulation, the resulting spatial surface deviations along the length of a member are obtained. Subsequent research aims to examine these imperfections' sensitivity to a CFS member's structural strength. A pristine finite element model of a CFS member is constructed. This 'perfect' model is then subjected to distortions by introducing simulated imperfections at corresponding nodes, as illustrated in Figure 10 [9]. This allows the impact of stochastically simulated imperfections to be explored using the traditional approach.

4.2. The 1D Spectral Simulation Method

The simulation using the 1D spectral method diverges from the traditional approach. Instead of attributing a single frequency to each corresponding mode of imperfection, the 1D spectral method assumes that each classified mode contains multiple frequencies, as depicted in Figure 11. To initiate the simulation, a series of base power spectra—corresponding to each imperfection mode—is generated by calculating the medians of the power spectra from the measured imperfections, as classified in Section 3.2. For further analysis, the amplitudes of the first five frequencies are retained. These frequencies are significant as they account for more than 70% of the energy in the classified imperfections.

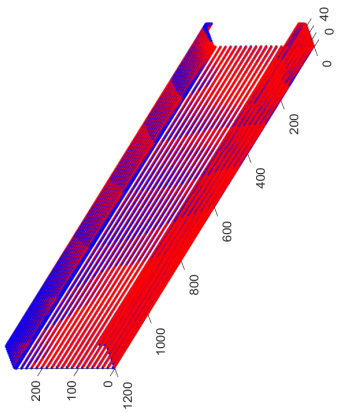

Figure 11. Imperfect model using the traditional approach.

The 1D spectral approach simulates imperfections based on the following Equations (8) and (9):

$$P(z) = \sum \alpha_i(z)\phi_i(x, y) \tag{8}$$

$$\alpha_i = \sum A_n \sin(w_n z + \varphi_n) \tag{9}$$

where:

α_i is the overall magnitude corresponding to imperfection mode i;
ϕ_i: represents the shape function corresponding to imperfection mode i;
A_n represents the magnitude of the term at a specific frequency w_n with respect to imperfection mode i;
w_n is the specific frequency, given by $w_n = 1/\lambda_n^i$;
φ_n is a random phase that is uniformly distributed over the interval $[0, 2\pi]$;
z denotes the longitudinal position of a simulated member;
n is a variable representing term of spectrum and is constrained within the set {1,2,3,4,5}.

(a) Magnitudes α_i

The overall magnitudes, α_i, are determined by the combined effect of the magnitudes at the first five frequencies, denoted as A_n, the frequency w_n, and the phase φ_n. Observations indicate that the spectral curves exhibit considerable similarity, and the normalized statistical values for a term magnitude A_n at any given frequency are consistently close. Consequently, Monte Carlo simulation is employed to generate A_n. The probabilistic model for each term is constructed based on the foundational spectrum curve presented in Figure 12.

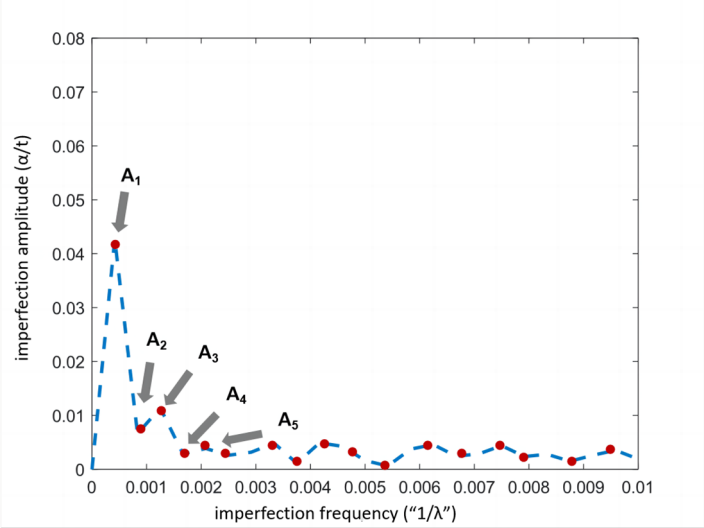

Figure 12. Typical base power spectrum curve of a mode imperfection.

In contrast to the traditional approach, which employs a coefficient of imperfection characteristics to govern the directionality of mode imperfections, the 1D spectral method incorporates the directionality within its multi-frequency sinusoidal function, facilitated by randomly generated phases. Specifically, the phase values for these sinusoidal functions are uniformly distributed over the interval $[0, \pi]$.

By stochastically simulating both term magnitudes and phases, the method captures the inherent variability of geometric imperfections that adhere to specific patterns. Unlike traditional approaches, which rely on linear superposition, the 1D spectral method embraces a more nuanced, nonlinear combination of mode imperfections.

(b) Shape function ϕ_i

In the 1D spectral method, the shape function ϕ_i slightly deviates from its definition in the traditional approach. The imperfection modes predominantly influence this function. To illustrate, the shape function for the local mode imperfection is derived by normalizing the cross-sectional deformation associated with local buckling in a CFS member. Similarly, for the CFS member (Figure 7), consistent shape functions are discernible for the distortional, bow, camber, and twist imperfection modes, as highlighted in Figure 10.

Imperfections are subsequently incorporated into a pristine perfect model by addition of displacements to points, as illustrated in Figure 13. A collapse analysis is then undertaken to examine the simulated imperfections that are discussed in Section 4.3.

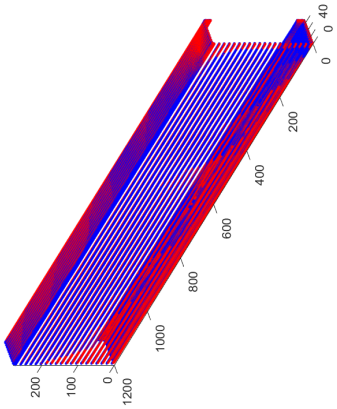

Figure 13. Spatial imperfections are created using the 1D spectral approach.

4.3. Analysis of Imperfection Simulations

The imperfection simulations approaches are compared through the strength prediction for compression CFS members through finite element analysis. Perfect cee-section models are first established, and the imperfections are added into nodes of the FE models.

The finite element models are built with the following parameters as shown in Table 3. The shell element S4R is used for mesh. The cross-sectional nodes are 58 and the longitudinal nodes are tenth of the length of a member, $L/10$. The boundary conditions are simply supports where displacement control is utilized for the loading. The '*Static, Stabilize' method is used in the analysis for the nonlinear deformation and inelastic performance of compression members. The validation of parameters has been discussed in previous research [23].

Table 3. Model parameter.

Material Property	Young's modulus/Mpa	Poisson's ratio	$\sigma_{0.2}$/Mpa	$\sigma_{0.5}$/Mpa	σ_{ult}/Mpa
	196,000	0.3	392	431	506
Step	Analysis method	Maximum number of steps	Initial increment	Minimum increment	Maximum increment
	*Static, Stabilize	300	0.001	1×10^{-5}	0.05
Mesh	Cross-section nodes	Longitude nodes [a]		Element type	
	58	$L/10$		S4R	
Boundary Condition	RP1 [b]			RP2 [c]	
	U1, U2, U3, UR1, UR3			U1, U3, UR1, UR3	

Note: [a] Different model lengths require different amounts of cross sections. L is the length of the member; the units of L are mm prime. [b] RP1 is the loading point located at the centroid of one end cross-section of members that ties nodes of the end cross-section, U1, U2, and U3 represent displacements that limit the X, Y, and Z axes, UR1, UR2, and UR3 represent limited rotation around the X, Y, and Z axes. [c] RP2 is another control point tie at the other end of the cross-section.

The material properties are tested through general material coupon testing which was presented in previous research [23]. The Young's modulus and Poisson's ratio are 196,000 Mpa and 0.3, respectively. The yield strength $\sigma_{0.2}$ and ultimate strength σ_{ult} are 392 MPa and 506 Mpa, respectively.

Both imperfection simulation approaches were applied to the specimens outlined in Table 1. For clarity, results from the section groups of CFS members, specifically C280-70-20, are showcased to highlight the differences between the simulation outcomes.

Spatial imperfections $P(z)$ for the C280-70-20 section groups are derived from measurements and incorporated into perfect finite element models. In these models, the thickness is set at 3 mm. The outcomes are presented in Table 3. Ten simulated imperfection samples are examined for each section group. Although stochastic imperfections may produce minor variations in peak loads, the overall statistical outcomes remain relatively consistent. Notably, the impact of the simulation approaches on the predicted peak loads for shorter members is minimal. For the L450-C280-70-20 model, the discrepancies between F_{trad} and F_{test} and F_{1D} and F_{test} are only 1.3% and 0.23%, respectively. This suggests that material properties rather than imperfections largely govern the performance of short columns. On the other hand, for the L1200-C280-70-20 section group, the differences between F_{trad} and F_{test} and F_{1D} and F_{test} are substantially greater—30.91% and 4.05%, respectively. This implies that the performance of medium-length columns is more challenging to predict due to the combined influences of imperfections and material properties, leading to larger deviations in simulation outcomes. For medium columns, cross-sectional imperfections play a pivotal role. The 1D spectral simulation method, with its ability to account for varying sinusoidal representations, offers a more accurate reflection of the real-world randomness of these imperfections. For the L3000-C280-70-20 section group, the discrepancies between F_{trad} and F_{test} and between F_{1D} and F_{test} are 10.22% and 4.64%, respectively. Global mode imperfections primarily influence slender columns, and both simulation approaches yield similar imperfection magnitudes. However, the 1D spectral method still provides a more precise prediction of the strength performance of CFS members.

The deformations of members in different simulations and testing are compared and a typical case is shown in Figure 14. It can be seen that the 1D spectral approach could better predict the deformation of members when it is compared with that of the traditional modal imperfection method.

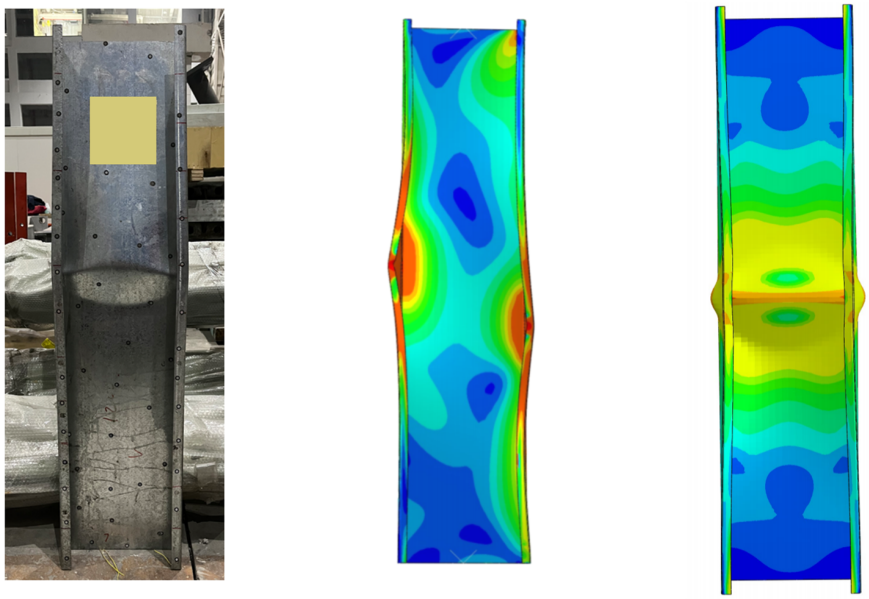

(**a**) (**b**) (**c**)

Figure 14. Failure modes validation for different simulation method: (**a**) Failure in testing; (**b**) Failure according to traditional modal method; (**c**) Failure according to 1D spectral method.

5. Influence of Mode Imperfections on Structural Strength

Although the real geometric imperfections of CFS members are complex and involve multiple mode imperfections, the simulation results presented in Section 4.3 indicate that specific mode imperfections may be dominant for different lengths of CFS members. Therefore, this section discusses the impact of single-mode imperfections on the section groups listed in Table 4: L450-C280-70-20, L1200-C280-70-20, L3000-C280-70-20. The thickness of these CFS members is 3 mm.

Table 4. Comparison of peak loads using different imperfection simulation approaches in collapse modeling.

		Traditional	1D Spectral	Testing	Difference (%)	
Section Group [b]		F_{trad}(kN)	F_{1D}(kN)	F_{test}(kN)	F_{trad} vs. F_{test}	F_{1D} vs. F_{test}
L450-C280-70-20 [a]	Mean	308.82	305.57	304.86	1.30%	0.23%
	Stdv.	0.61	1.34			
L1200-C280-70-20	Mean	185.29	147.27	141.54	30.91%	4.05%
	Stdv.	2.03	0.91			
L3000-C280-70-20	Mean	82.81	71.65	75.13	10.22%	4.64%
	Stdv.	1.86	0.47			

Note: [a] Each member in the section group has a thickness of 3 mm. [b] A set of 10 samples was used for each simulation within the section group.

Based on the statistical values of geometric imperfections presented in Table 2, the magnitudes of different mode imperfections are randomly generated and shown in Table 5. Equations (8) and (9) can also applied to simulate single-mode imperfections by setting the magnitudes of other imperfections to zero.

Table 5. Randomly generated mode imperfections.

CFS Members	Imperfection Mode				
	G_1(mm)	G_2(mm)	G_3(rad)	d_1(mm)	d_2(mm)
450 mm	0.05	0.03	0.0007	−0.54	0.12
1200 mm	0.16	0.08	0.0023	0.28	0.29
3000 mm	1.09	0.83	0.0026	0.38	0.15

Spatial imperfections generated from simulations are superimposed onto the perfect finite element models, as described in Section 4.3. The results are presented in Table 6. For the short columns measuring 450 mm in length (as seen in Table 6), the influence of geometric imperfections on strength is particularly pronounced, especially for cross-sectional imperfections. The global mode imperfection, G1, has a more dominant effect compared to other mode imperfections, with a difference of 1.9%. While single-mode imperfections can affect the ultimate load capacity of a CFS member, the combined effect of multiple geometric imperfections can counteract the impact of individual modes.

For medium columns measuring 1200 mm in length (as referenced in Table 6), the most influential mode imperfections are the local mode and twist, with differences of 0.3% and 0.6%, respectively. Nonetheless, the contributions from geometric imperfections are relatively uniformly distributed. The most significant variance observed is 1.6% for the G2 mode imperfection.

For slender columns measuring 3000 mm in length (as shown in Table 6), the most influential mode imperfections are the global G1 imperfections, with an impact difference of 2.5%. This outcome aligns with the general understanding that G1 mode imperfections adversely affect the strength of CFS members to the greatest extent.

Table 6. Simulation and experimental results for single mode imperfections.

L450-C280-70-20-3			
Modes	**Model F_{sg}(kN)**	**Testing F_{test} (kN)**	**Impacts (%)**
G_1	310.77	304.86	1.9
G_2	297.29		2.5
G_3	296.9		2.6
d_1	297.23		2.5
d_2	320.41		5.1
L1200-C280-70-20-3			
Modes	**Model F_{sg}(kN)**	**Testing F_{test} (kN)**	**Impacts (%)**
G_1	143.26	141.539	1.20%
G_2	143.08		1.60%
G_3	142.38		0.60%
d_1	141.95		0.30%
d_2	143.6		1.50%
L3000-C280-70-20-3			
Modes	**Model F_{sg}(kN)**	**Testing F_{test} (kN)**	**Impacts (%)**
G_1	73.25	75.13	2.50%
G_2	71.8		4.40%
G_3	72.13		4.00%
d_1	71.45		4.90%
d_2	71.61		4.70%

6. Conclusions

This paper introduces a newly developed machine-vision imperfection inspection technique for cee-section CFS members that automates the characterization of mode imperfections from measurements of a hand-held laser scanner. Two simulations of imperfections are insightfully studied with validation of testing results. The contributions of imperfection modes are carefully studied, and the conclusions are as follows:

1. A machine-vision imperfection inspection technique is developed where an automatic imperfection characterization algorithm is implemented for CFS members. The characterization algorithm normalizes the buckling mode shapes from CFSM research and recognizes corresponding magnitudes of surface deviations from scanning. The easiness and efficiency of machine-vision imperfection inspection leverages the application of geometric imperfection study;
2. The characterized mode imperfections have been statistically analyzed. Most importantly, the imperfections are compared with past measurement data which show great similarity, especially in cross-section mode imperfections, and G2 and G3 global mode imperfections. The similarity indicates the probabilistic models of mode imperfections from the statistical analysis can be leveraged in other research where imperfections of cee-section CFS members are needed;
3. Two imperfection simulations methods are compared, i.e., traditional modal imperfection approaches and 1D spectral mode imperfections. Testing results are used to validate finite element analysis with two different mode imperfections. The results show that 1D spectral mode imperfections can better predict behaviors of cee-section CFS members from the point of view of both loading capacity and deformation;
4. The study also dives deep into single-mode imperfections, analyzing their respective contributions to the strength of cee-shaped CFS members. The findings suggest that short columns exhibit minimal impacts from imperfections, while medium columns are influenced by the twist (G3) and local mode imperfections. On the other hand, slender columns predominantly showcase susceptibilities to the bow imperfection (G1).

The 1D spectral method can accommodate both stochasticity and applicability in numerical simulation of CFS members. The base spectrum curves can generate multiple-frequency imperfection longitudinal waves for a given mode imperfection with random phases. On the other hand, 70% of the imperfection energy is accounted for in the first five terms of the spectrum at a specific pattern. The base spectrum for general applications can be developed in future research involving more shapes of CFS members. Furthermore, the contributions of mode imperfections should be evaluated so that weighting of different mode imperfections can be considered with respect to the length of CFS members.

Author Contributions: Conceptualization, X.Z.; methodology, H.G. and X.Z.; validation, X.S. and H.G.; data analysis, X.S. and X.Z.; data curation, X.Z.; writing—original draft, X.Z.; writing—review and editing, X.Z. and P.D.; visualization, H.G.; supervision, H.G.; funding acquisition, X.Z. and H.G. All authors have read and agreed to the published version of the manuscript.

Funding: This research was funded by the Ministry of Housing and Urban-Rural Development Science and Technology Plan Project, with the grant number 2020-K-094, and by the Youth Program of the National Natural Science Foundation of China under grant number 52208141.

Data Availability Statement: The data used in this study will be made available upon request.

Acknowledgments: This research was primarily funded by the Ministry of Housing and Urban-Rural Development Science and Technology Plan Project, Grant No. 2020-K-094. Additional support was provided by the Youth Program of the National Natural Science Foundation of China, Grant No. 52208141, and the Beijing Energy Conservation and Sustainable Urban and Rural Development Provincial and Ministry Co-construction Collaboration Innovation Center. The opinions, findings, conclusions, or recommendations presented in this material are solely those of the authors and do not necessarily reflect the views of the sponsors or other affiliated entities.

Conflicts of Interest: The authors declare no conflict of interest.

References

1. Zhao, X.; Tootkaboni, M.; Schafer, B. Development of a laser-based geometric imperfection measurement platform with application to cold-formed steel construction. *Exp. Mech.* **2015**, *55*, 1779–1790. [CrossRef]
2. Zeinoddini, V.M.; Schafer, B.W. Simulation of geometric imperfections in cold-formed steel members using spectral representation approach. *Thin-Walled Struct.* **2012**, *60*, 105–117. [CrossRef]
3. Winter, G. Strength of thin steel compression flanges. *Trans. Am. Soc. Civ. Eng.* **1947**, *112*, 527–554. [CrossRef]
4. Chatterjee, A.; Arwade, S.R.; Schafer, B.W.; Moen, C.D. System reliability of floor diaphragms framed from cold-formed steel with wood sheathing. *J. Struct. Eng.* **2018**, *04017208*, 144. [CrossRef]
5. Liu, W.; Zhang, H.; Rasmussen, K. System reliability-based Direct Design Method for space frames with cold–formed steel hollow sections. *Eng. Struct.* **2018**, *166*, 79–92. [CrossRef]
6. Zeinoddini, V.; Schafer, B.W. Global imperfections and dimensional variations in cold-formed steel members. *Int. J. Struct. Stab. Dyn.* **2011**, *11*, 829–854. [CrossRef]
7. Farzanian, S.; Louhghalam, A.; Schafer, B.W.; Tootkaboni, M. Geometric imperfections in CFS structural members, Part II: Data-driven modeling and probabilistic validation. *Thin-Walled Struct.* **2023**, *185*, 110620. [CrossRef]
8. Farzanian, S.; Louhghalam, A.; Schafer, B.W.; Tootkaboni, M. Geometric imperfections in CFS structural members: Part I: A review of the basics and some modeling strategies. *Thin-Walled Struct.* **2023**, *186*, 110619. [CrossRef]
9. Zhao, X.; Wang, G.; Sun, X.; Wang, X.; Schafer, B. Modeling of uncertain geometry of cold formed steel members based on laser measurements and machine learning. *Eng. Struct.* **2023**, *115578*, 279. [CrossRef]
10. Aktepe, R.; Erkal, B.G. State-of-the-art review on measurement techniques and numerical modeling of geometric imperfections in cold-formed steel members. *J. Constr. Steel Res.* **2023**, *207*, 107942. [CrossRef]
11. Schafer, B.; Pekoz, T. Computational modeling of cold-formed steel: Characterizing geometric imperfections and residual stresses. *J. Constr. Steel Res.* **1998**, *47*, 193–210. [CrossRef]
12. Young, B.; Rasmussen, K. Measurement techniques in the testing of thin-walled. *Exp. Mech.* **2003**, *43*, 32–38. [CrossRef]
13. Peterman, K. *Behavior of Full-Scale Cold-Formed Steel Building under Seismic Excitations*; Johns Hopkins University: Baltimore, MD, USA, 2014.
14. McAnallen, L.E.; Padilla-Llano, D.A.; Zhao, X.; Moen, C.D.; Schafer, B.W.; Eatherton, M.R. Initial geometric imperfection measurement and characterization of cold-formed steel c-section structural members with 3D non-contact measurement techniques. In Proceedings of the AISC Annual Stability Conference, Toronto, ON, Canada, 27 August 2014.
15. Vieira, L.C.M., Jr.; Shifferaw, Y.; Schafer, B.W. Experiments on sheathed cold-formed steel studs in compression. *J. Constr. Steel Res.* **2011**, *67*, 1554–1566. [CrossRef]

16. Xu, D.; Wang, Y.; Liu, X.; Chen, B.; Bu, Y. A novel method and modelling technique for determining the initial geometric imperfection of steel members using 3D scanning. *Structures* **2023**, *49*, 855–874. [CrossRef]
17. Zhang, Z.; Shi, G.; Hou, L.; Zhou, L. Geometric dimension and imperfection measurements of box-T section columns using 3D scanning. *J. Constr. Steel Res.* **2021**, *106742*, 183. [CrossRef]
18. Li, Z.; Ádány, S.; Schafer, B.W. Modal identification for shell finite element models of thin-walled members in nonlinear collapse analysis. *Thin-Walled Struct.* **2013**, *67*, 15–24. [CrossRef]
19. Zhao, X.; Tootkaboni, M.; Schafer, B. Laser-based cross-section measurement of cold-formed steel members: Model reconstruction and application. *Thin-Walled Struct.* **2017**, *120*, 70–80. [CrossRef]
20. Erkal, B.G.; Çağrıcı, Ö.G. Automated geometric imperfection detection and quantification of CFS members from point clouds. *KSCE J. Civ. Eng.* **2022**, *26*, 3888–3904. [CrossRef]
21. Dinis, P.B.; Camotim, D. Local/distortional mode interaction in cold-formed steel lipped channel beams. *Thin-Walled Struct.* **2010**, *48*, 771–785. [CrossRef]
22. SHINING 3D. EinScan HX. Available online: https://www.einscan.com/einscan-hx/.QuickGuide (accessed on 26 October 2023).
23. Du, P.; Zhao, X.; Zhang, Z.; Sun, X.; Du, G. Digital Twin-Based Numerical Simulation Method for Cee-Shape Cold-Formed Steel Members. *Buildings* **2023**, *13*, 2388. [CrossRef]
24. American Iron and Steel Institute. *North American Specification for the Design of Cold-Formed Steel Structural Members: AISI S100-2016*; American Iron and Steel Institute: Washington, DC, USA, 2016.
25. *G. 50017*; Steel Structure Design Standard. China Construction Industry Press: Beijing, China, 2017.
26. Shifferaw, Y.; Vieira, L.C.M., Jr.; Schafer, B.W. Compression testing of cold-formed steel columns with different sheathing configurations. In Proceedings of the Structural Stability Research Council—Annual Stability Conference, Atlanta, GA, USA, 21–24 April 2020; pp. 593–612.
27. Xu, J.; Xing, K.; Gao, X. Experimental investigation on compressive bearing capacity of cold-formed thin-walled lipped channel short columns with corrosion. *Eng. Mech.* **2021**, *38*, 191–199.
28. Wang, C.; Zhang, Y.; Zhang, Z. Experimental investigation on channel columns with inclined simple edge stiffeners under compression loading. *J. Build. Struct.* **2006**, *1*, 312–321.